

An in vivo validation dataset for dynamic volumetric MRI

Max H.C. van Riel^{*1}, David G.J. Heesterbeek¹, Martijn Froeling², Cornelis A.T. van den Berg¹, and Alessandro Sbrizzi¹

¹Computational Imaging Group for MRI Therapy & Diagnostics, Department of Radiotherapy, University Medical Center Utrecht, Utrecht, The Netherlands

²Precision Imaging Group, Department of Radiology, University Medical Center Utrecht, Utrecht, The Netherlands

Abstract

Dynamic volumetric MRI provides valuable information on in vivo motion and biomechanics, with applications spanning cardiac, musculoskeletal, or pulmonary imaging, amongst others. Developing reconstruction methods for time-resolved volumetric MRI is challenging due to the inherently slow acquisition process of MRI, which makes it an active area of research. However, in vivo validation of these methods remains challenging due to the lack of publicly available datasets with fully sampled ground-truth images. Here, we present a publicly available in vivo dataset designed to facilitate the development and validation of dynamic volumetric MRI reconstruction algorithms. Controlled and repeatable deformations of the muscles in the thigh were induced using a pneumatic pressure cuff, enabling the acquisition of both undersampled dynamic data and fully sampled validation images. The dataset comprises multichannel undersampled k-space data from nine healthy volunteers across four different dynamic deformations, with fully sampled validation data for one deformation. Additionally, an anatomical reference scan and muscle segmentation masks are provided for each subject. To illustrate a possible image reconstruction and validation approach, a binning-based reconstruction was performed on the undersampled data from six dynamic repetitions. The resulting images were consistent with the corresponding fully sampled validation images. This dataset offers possibilities for validating and advancing time-resolved volumetric MRI reconstruction methods.

1 Background & Summary

Magnetic resonance imaging (MRI) is a widely-used imaging modality with excellent soft-tissue contrast. It enables noninvasive assessment of anatomical and physiological properties of the human body. Conventional MRI acquisitions are typically performed under static conditions, where any motion is considered an artifact that has to be mitigated¹. However, dynamic imaging and motion quantification can also serve as a valuable source of information. Dynamic MRI techniques aim to capture and quantify in vivo motion and biomechanics, with a broad range of clinical and research applications. For instance, dynamic MRI of the heart enables the estimation of biomarkers such as left ventricular ejection fraction and myocardial strain, which are critical for diagnosing and monitoring cardiovascular diseases^{2,3}. Similarly, dynamic MRI can be used to characterize muscle tissue properties^{4,5}, assess pulmonary ventilation and perfusion⁶, investigate motion of the vocal tract for speech MRI⁷, and capture gastrointestinal motility^{8,9}.

A key challenge in dynamic MRI is the inherently slow acquisition process of MRI. MRI scanners measure data in the spatial frequency domain, called k-space. The signal in k-space needs to be sampled at the Nyquist rate to prevent aliasing artifacts. Only after all required k-space samples have been acquired can an image be reconstructed using the inverse Fourier transform. Acceleration of the data acquisition by undersampling the data, combined with advanced reconstruction techniques, is crucial to reduce scan time for static imaging, or to increase the temporal resolution for dynamic imaging. These

^{*}Corresponding author: m.h.c.vanriel-3@umcutrecht.nl

acceleration strategies include parallel imaging using multiple receive coils, compressed sensing using sparsity-promoting priors such as total variation or wavelet transforms, and low-rank constraints^{10–14}.

A common problem for dynamic 2D (2D+t) methods is through-slice motion, since most physiological motion is inherently three-dimensional. Therefore, dynamic volumetric (3D+t) imaging methods are preferred, since they are capable of completely capturing the dynamic processes. However, acquiring fully sampled 3D+t data at sufficient spatio-temporal resolutions is not feasible. Current approaches often acquire data over multiple motion cycles, combining data from these repetitions into several motion bins to reconstruct a single representative cycle^{15–17}. This binning strategy requires consistent periodic motion, but achieving accurate repeatability of the motion is complicated in many dynamic imaging applications. In cardiac applications for example, this is problematic when arrhythmias occur, or when patients have difficulties holding their breath¹⁸. Accurate repeatability of the motion is also complicated for other dynamic imaging applications, such as dynamic muscle imaging, where accurate repetitive motion is hard to achieve. Therefore, the development of robust acquisition and reconstruction techniques for time-resolved 3D+t MRI that do not rely on the periodicity of the motion remains an active area of research^{19–21}.

When developing 3D+t MRI methods, it is important to have access to ground-truth data to validate the reconstruction results. Currently, there are some 2D+t datasets available that provide fully sampled data, which can be retrospectively undersampled^{22,23}. The reconstruction from the undersampled data can then be compared to the ground-truth reconstruction using the fully sampled data. However, there is a lack of publicly available 3D+t datasets with fully sampled ground-truth images that enable the validation of 3D+t reconstruction methods.

In this work, we present a publicly available in vivo dataset designed to support research in 3D+t MRI reconstruction methods. We have created a controllable setup to induce repeatable deformations in the thigh muscles. The dataset contains multichannel undersampled k-space data acquired from nine healthy volunteers. Four distinct dynamic deformations are included for each subject. For the first of these deformations, fully sampled data is also available, enabling validation of the reconstructed 3D+t images. In addition to dynamic image reconstruction, the dataset enables analysis of strain and stiffness, as demonstrated in prior work for a single subject^{24,25}.

2 Methods

2.1 Experimental setup

To enable the acquisition of validation data, a setup that allows for controllable deformations was realized. A pneumatic cuff from a manual blood pressure monitor was positioned around the right thigh of a healthy volunteer (Figure 1). The pressure within the cuff was regulated using a manual pump and monitored via an analog pressure gauge (in mmHg). Gradual inflation of the cuff applied an external compressive force on the subject’s thigh, inducing time-dependent deformations of the muscles. A long plastic pneumatic tube connected the cuff to the pump and the pressure gauge, allowing for remote operation outside the MRI scanner room. This simple setup enabled the acquisition of undersampled data in a dynamic setting, as well as fully sampled validation images, as explained below.

2.2 MRI data acquisition

All MRI imaging was performed on a 1.5T MRI system (Ingenia, Philips Healthcare, Best, The Netherlands). The study was approved by the Institutional Review Board of the UMC Utrecht. Nine healthy volunteers (3F/6M) were included after giving informed consent for anonymized data sharing. Subjects were placed in supine (face-up), feet-first position in the scanner, with the pressure cuff placed around their right thigh. Their knees were supported to minimize bulk motion during and between the scans. A 16-channel anterior coil and a 12-channel posterior coil (integrated in the table) were used for data acquisition.

For each subject, the following scans were acquired: one anatomical reference scan, one DIXON scan, one validation scan, one hybrid dynamic and validation scan, and four dynamic scans. All scans apart from the DIXON scan were acquired with an RF-spoiled gradient echo sequence, using a repetition time (TR, i.e. the time between two successive radiofrequency pulses) of 5.4 ms, and an echo time (TE, i.e.

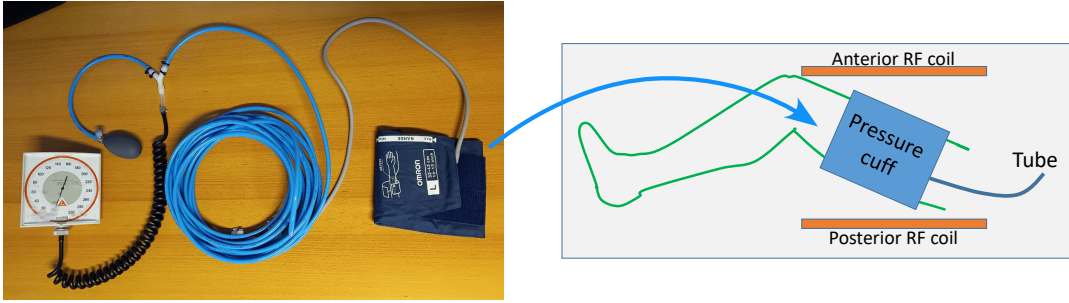


Figure 1: Experimental setup, from left to right: pressure gauge, hand pump, long tube (allowing operation outside of the scanner room), and pressure cuff, which is placed around the thigh of the volunteer.

the time between the radiofrequency pulse and the readout) of 2.3 ms. At this particular echo time, water and fat have opposite phase, producing dark bands at muscle boundaries that enhance segmentation and motion detection.

2.2.1 Anatomical reference and segmentation

As an anatomical reference, a high-resolution static scan was acquired without deformations at a resolution of 1.5 mm in each direction. This scan shows finer anatomical details than the dynamic data. Additionally, a DIXON scan was acquired with three echo times (1.20 ms, 2.67 ms, and 4.14 ms), from which muscle segmentation masks could be generated.

2.2.2 Validation data

Fully sampled validation images were acquired at nine discrete pressure levels. The pressure cuff was inflated from 0 to 80 mmHg and deflated back to 0 mmHg in 20 mmHg increments, where the pressure was kept constant at each increment for 22 seconds to acquire a fully sampled validation image (Figure 2). The k -space was sampled on a grid of 128-by-64-by-64 with an isotropic spatial resolution of 3.5 mm. During each TR, one readout line (128 samples) along the k_x -direction was acquired. The k_y - k_z plane was sampled using a conventional linear sampling pattern (Figure 3).

In addition, a single repetition of the pressure cycle was performed: the pressure cuff was continuously inflated from 0 mmHg (no deformation) to 80 mmHg (maximum deformation), where the pressure was sustained for 20 seconds, and subsequently deflated back to 0 mmHg. This resulted in a hybrid dataset containing both dynamic and validation data, where the dynamic part can be used for a time-resolved reconstruction, whereas the data acquired while the pressure was sustained can be used to generate one validation image at maximal deformation. The k -space was sampled on the same grid as the validation data, but during this scan, the readouts were sampled using Cartesian acquisition with spiral profile order (CASPR)²⁶ in the k_y - k_z plane, with 32 readouts per spiral shot (Figure 3). This sampling strategy combines the benefits of non-Cartesian sampling, like the oversampling of the k -space center, with the robustness of Cartesian sampling against field inhomogeneities, gradient delays, and eddy currents.

2.2.3 Dynamic data

During the dynamic scans, the pressure cuff was inflated from 0 mmHg (no deformation) to 80 mmHg (maximum deformation) and immediately deflated back to 0 mmHg. This pressure cycle resulted in repeatable elastic deformations of the muscles.

For each subject, four dynamic scans were performed (Figure 2):

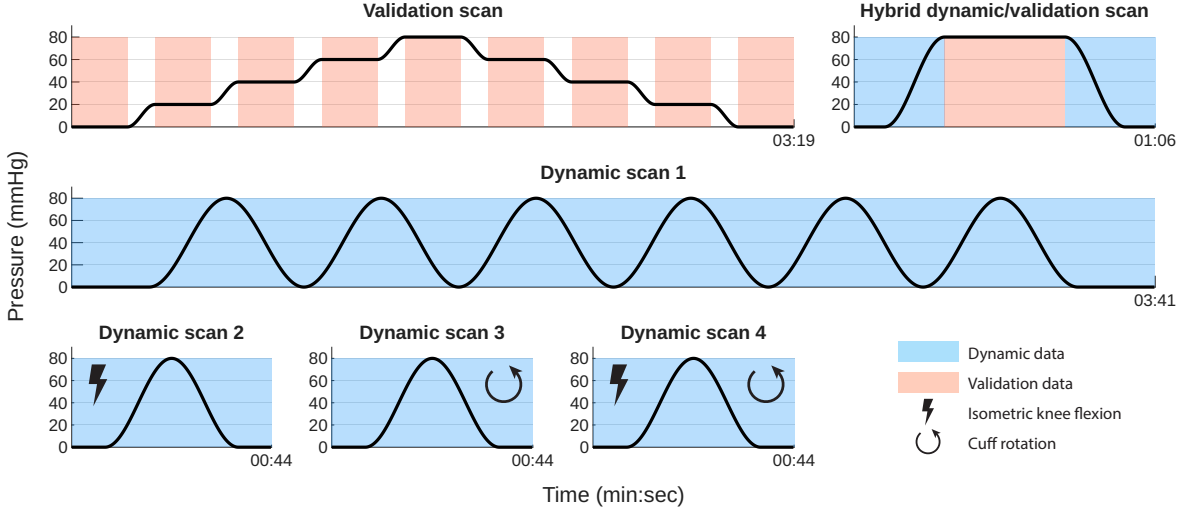


Figure 2: Pressure profiles for the validation scans and the dynamic scans. Data acquired during the blue-shaded time intervals can be used for dynamic time-resolved reconstructions, while data acquired during the orange-shaded time intervals can serve as validation data for the dynamic reconstructions. Dynamic scans 2 and 4 were acquired during an isometric knee flexion task. During dynamic scans 3 and 4 the pressure cuff was rotated. The acquisition time for each scan is indicated on the horizontal axis.

1. Six consecutive repetitions of the pressure cycle at 35-second intervals.
2. A single pressure cycle, during which the volunteer was asked to press their heel into the scanner table. This activated the muscles in the posterior (back) side of the leg, which are responsible for bending the knee joint, leading to isometric flexion of the knee.
3. The pressure cuff was repositioned at a different angle around the thigh and a single pressure cycle was performed. This changed the pressure distribution around the leg, thus changing the deformation patterns in the muscles.
4. The isometric knee flexion task of dynamic scan 3 was repeated with the rotated pressure cuff.

All four dynamic scans were acquired using the CASPR sampling pattern (Figure 3).

2.3 Image reconstruction

For the scans with fully sampled data, an image was reconstructed using the inverse Fourier transform followed by a sensitivity-weighted combination over the receive channels:

$$\rho(\mathbf{x}) = \frac{1}{\sum_l^{N_c} c_l^*(\mathbf{x}) c_l(\mathbf{x})} \sum_j^{N_c} c_j^*(\mathbf{x}) \mathcal{F}^{-1}[s_j(\mathbf{k})], \quad (1)$$

with $\rho(\mathbf{x})$ the image intensity at location \mathbf{x} , $s_j(\mathbf{k})$ the k-space signal from the j -th channel at k-space coordinate \mathbf{k} , \mathcal{F}^{-1} the inverse Fourier transform, $c_j(\mathbf{x})$ the coil sensitivity of the j -th receive channel, N_c the number of receive channels, and $*$ indicating complex conjugation. The coil sensitivity maps were determined from a separate prescan and are also included in the dataset.

2.4 Muscle segmentations

The out-of-phase images from the DIXON scan were converted from Digital Imaging and Communications in Medicine (DICOM) to Neuroimaging Informatics Technology Initiative (NIFTI) file format using dcm2niix v1.0.20250505²⁷. Muscle segmentations were generated from these NIFTI files using a

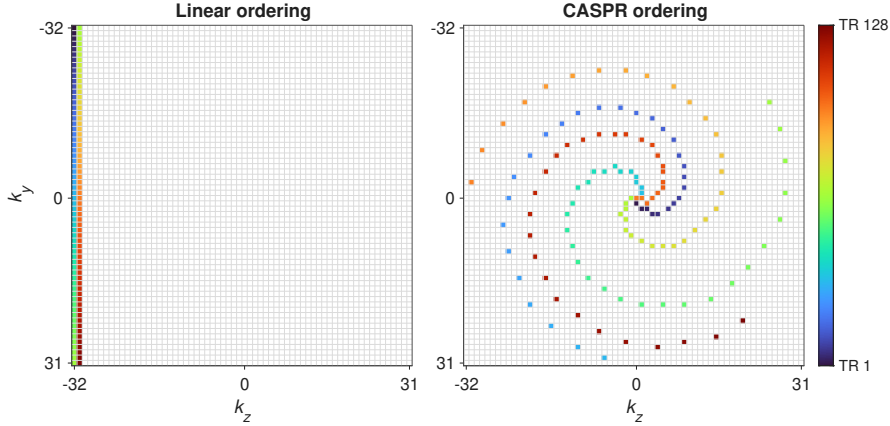


Figure 3: Left: Regular linear sampling pattern, as used for the static validation data. Right: CASPR sampling pattern, as used for the dynamic data and the hybrid dynamic/validation data. The readout direction (k_x , not shown) is perpendicular to the figure. The colors indicate the sampling order for the first 128 readouts.

pretrained U-net²⁸ as implemented in QMRITools 4.2.8²⁹. These segmentation masks were visually checked and where necessary corrected using ITK-SNAP 4.0.1.

3 Data Records

The data can be found at doi.org/10.5281/zenodo.18459637. All datasets are saved in the ISMRMRD file format³⁰. For each subject, the following files are available:

- `anatomy.nii.gz`: High-resolution fully sampled anatomical reference image
- `outphase.nii.gz`: Out-of-phase image from the DIXON scan
- `segmentation.nii.gz`: Muscle segmentation masks as determined from the out-of-phase image; each voxel is assigned an integer corresponding to a certain segmentation label
- `segmentation.txt`: Label descriptions of the segmentation masks
- `validation.mrd`: Fully sampled multichannel k-space data for each of the nine pressure levels
- `hybrid.mrd`: Multichannel k-space data for the hybrid dynamic and validation scan
- `dynamic1.mrd`, ..., `dynamic4.mrd`: Undersampled multichannel k-space data for the four dynamic scans

The only preprocessing performed to the raw k-space data is the removal of the oversampling in the readout direction, as this reduces the size of the dataset by a factor 2. In addition to the k-space data, each data file containing raw k-space data also contains noise measurements, required for prewhitening the data. Each `.mrd` file is a HDF5 file that contains the raw k-space and noise data in MRD format in `/dataset/data`, the MRD header in `/dataset/xml`, and the coil sensitivity maps in `/csm`.

4 Data Overview

Figure 4 shows representative images for a single volunteer that can be reconstructed from the dataset using the direct image reconstruction given by equation (1). Note that we used the radiological convention to display the images, which means that the right leg is shown on the left side of the image.

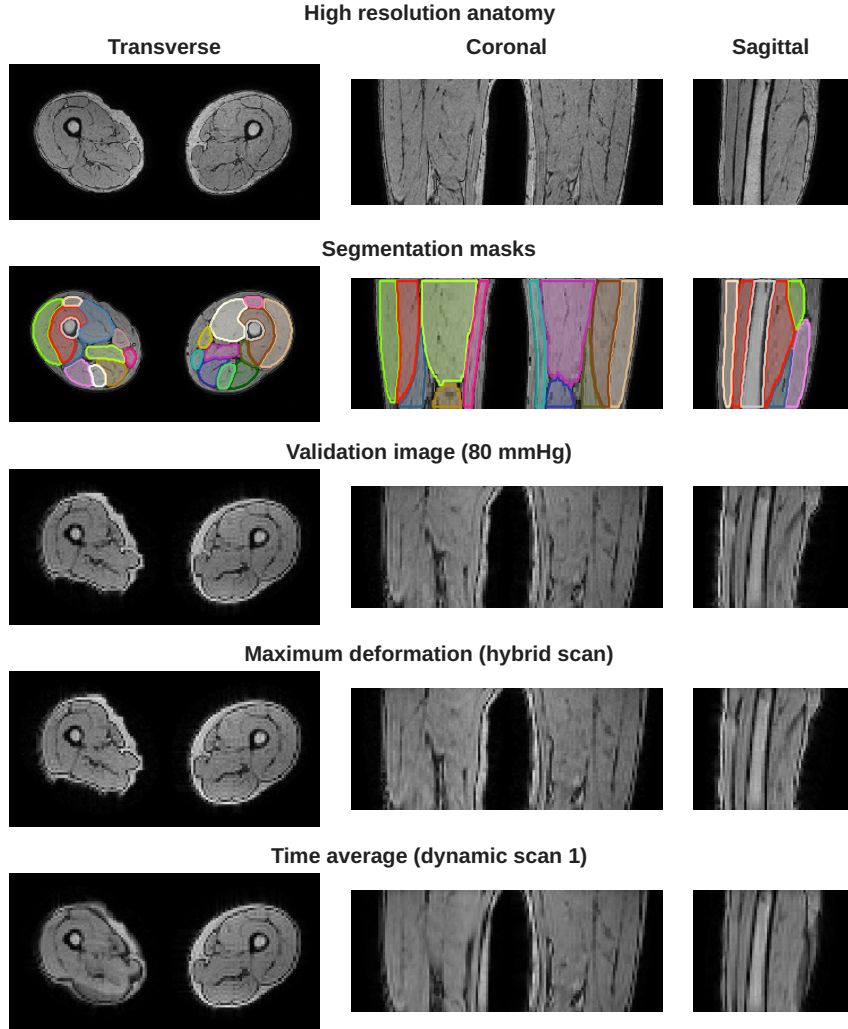


Figure 4: Overview of the different scans in the dataset. From top to bottom: high-resolution anatomical image; out-of-phase image from the DIXON scan with the muscle segmentation masks overlaid; fifth validation image from the static validation data (at the maximum pressure level of 80 mmHg); image at the maximum deformation reconstructed from the validation part of the hybrid dynamic/validation scan; time-averaged image from the data of all six dynamic repetitions of dynamic scan 1. Note that due to the radiological convention, the right leg is shown on the left side of the transverse and coronal images.

5 Technical Validation

Direct reconstructions of time-resolved images from the undersampled k-space data would result in severe artifacts (like the motion artifacts in the time-averaged reconstruction in Figure 4), unless advanced reconstruction algorithms are used, which is beyond the scope of this data descriptor. Nevertheless, we can still reconstruct motion-resolved images from dynamic scan 1 using a binning strategy. Note that this approach is not time-resolved, since it uses the data from multiple dynamic repetitions and thus assumes periodicity of the motion.

Each pseudo-spiral shot of the CASPR sampling pattern begins by sampling the line through the center of k-space. A 1D inverse Fourier transform yields the projection of the imaging data on the x -axis (the readout direction). This projection changes as the image deforms, and thus can be used as a surrogate signal that shows the motion that happened during the scan. Using the correlation

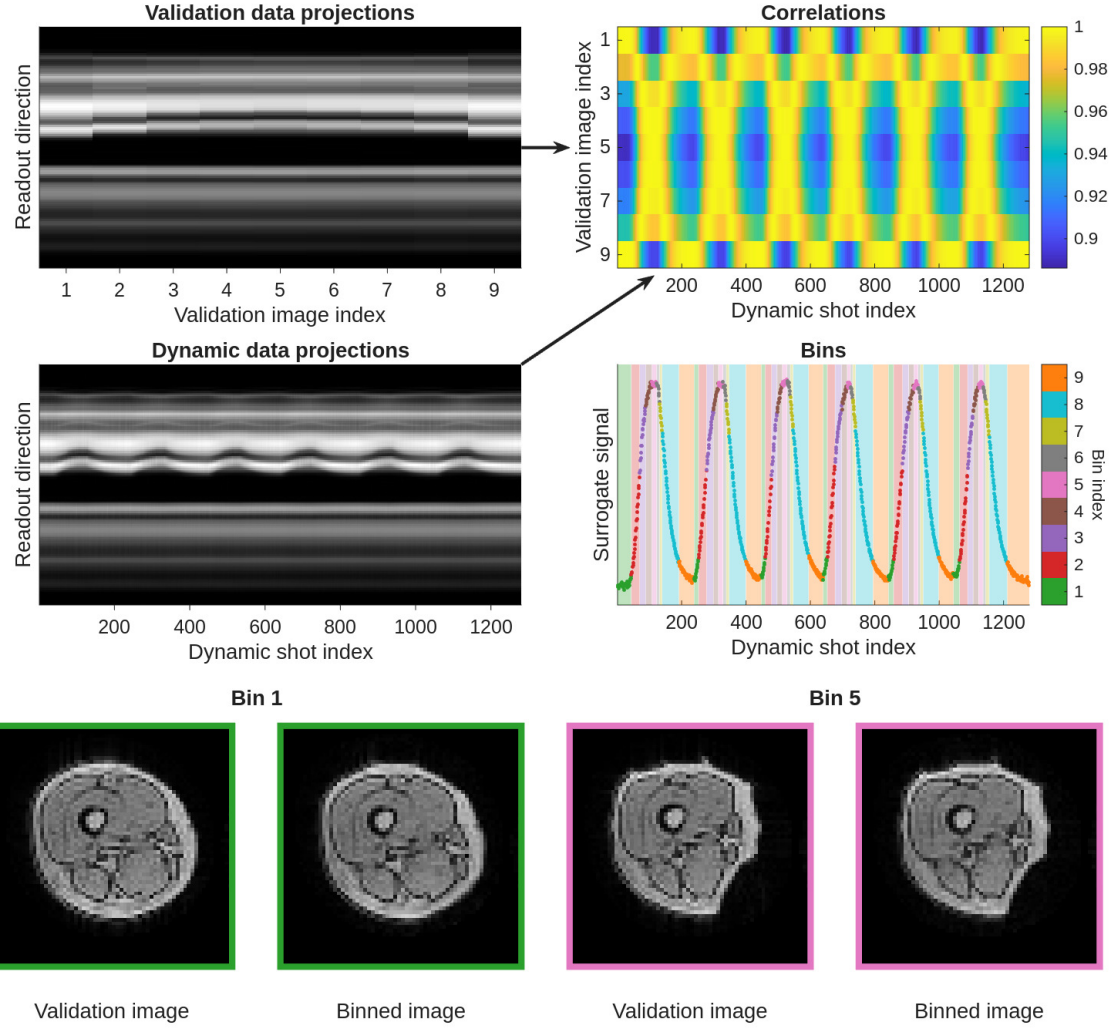


Figure 5: Binned image reconstruction approach. Projections on the readout axis are calculated for each validation image and each CASPR shot of dynamic scan 1. The correlations between these projections are then used to divide the shots into nine bins, with each bin corresponding to one validation image. The first principal component of the projection data is used as motion surrogate signal. The validation images and corresponding images from the binning strategy are shown for bin 1 (no deformation) and bin 5 (maximal deformation).

between the surrogate signals of the dynamic scan and those of the validation scan, the data from the six repetitions of dynamic scan 1 can be grouped into nine bins, with each bin corresponding to one of the nine validation images. Each bin is only slightly undersampled, allowing image reconstruction via a regularized parallel imaging reconstruction, as implemented in BART 0.9³¹. The resulting images of this binned reconstruction show high similarity to the corresponding validation images (Figure 5), confirming that the induced deformations during the dynamic scans were consistent with those observed in the validation scan.

6 Usage Notes

When combining data from different scans, users of the dataset should be aware that there may be minor positional shifts of the leg between scans. This could be caused by the repositioning of the pressure cuff, or by the subject moving their leg during the isometric knee flexion tasks. Therefore, coil sensitivities

were determined for each scan separately, as these may be different across different scans.

Furthermore, when using the segmentation masks, a nonrigid registration between the out-of-phase DIXON image (on which the segmentation was performed) and an image of the target reconstruction (for example, the first frame) is recommended. In addition, a minor misalignment might appear when comparing the validation images to reconstructed images from one of the dynamic scans. Only rigid registration should be performed in this case to prevent warping the validation or reconstructed images. Since both legs can move independently, we advise cropping out the right leg in both images, followed by a rigid registration.

The left leg does not deform, and can thus be used as a control to compare against. Note the absence of motion artifacts in the left leg (right side of the image) in the time-averaged image in Figure 4, and the constant projections in Figure 5.

7 Data availability

The dataset is publicly available on Zenodo at doi.org/10.5281/zenodo.18459637.

8 Code availability

An example script that loads the data, preprocesses the raw data, and performs a basic image reconstruction is included in the dataset.

Funding

This research was supported by the Dutch Research Council (NWO), grant 18897.

References

- [1] Zaitsev, M., Maclaren, J. & Herbst, M. Motion artifacts in MRI: A complex problem with many partial solutions. *J. Magn. Reson. Imaging* **42**(4), 887–901 (2015). doi:10.1002/jmri.24850.
- [2] Puntmann, V. O., Valbuena, S., Hinojar, R., Petersen, S. E., Greenwood, J. P., Kramer, C. M., Kwong, R. Y., McCann, G. P., Berry, C., Nagel, E. & SCMR Clinical Trial Writing Group. Society for Cardiovascular Magnetic Resonance (SCMR) expert consensus for CMR imaging endpoints in clinical research: part I - analytical validation and clinical qualification. *Journal of Cardiovascular Magnetic Resonance* **20**(1), 67 (2018). doi:10.1186/s12968-018-0484-5.
- [3] Amzulescu, M. S., De Craene, M., Langet, H., Pasquet, A., Vancraeynest, D., Pouleur, A. C., Vanoverschelde, J. L. & Gerber, B. L. Myocardial strain imaging: review of general principles, validation, and sources of discrepancies. *European Heart Journal - Cardiovascular Imaging* **20**(6), 605–619 (2019). doi:10.1093/ehjci/jez041.
- [4] Sinha, U., Malis, V., Csapo, R., Moghadasi, A., Kinugasa, R. & Sinha, S. Age-related differences in strain rate tensor of the medial gastrocnemius muscle during passive plantarflexion and active isometric contraction using velocity encoded MR imaging: Potential index of lateral force transmission. *Magn. Reson. Med.* **73**(5), 1852–1863 (2015). doi:10.1002/mrm.25312.
- [5] Mazzoli, V., Gottwald, L. M., Peper, E. S., Froeling, M., Coolen, B. F., Verdonschot, N., Sprengers, A. M., van Ooij, P., Strijkers, G. J. & Nederveen, A. J. Accelerated 4D phase contrast MRI in skeletal muscle contraction. *Magn. Reson. Med.* **80**(5), 1799–1811 (2018). doi:10.1002/mrm.27158.
- [6] Ilicak, E., Ozdemir, S., Zapp, J., Schad, L. R. & Zöllner, F. G. Dynamic mode decomposition of dynamic MRI for assessment of pulmonary ventilation and perfusion. *Magn. Reson. Med.* **90**(2), 761–769 (2023). doi:10.1002/mrm.29656.
- [7] Scott, A. D., Wylezinska, M., Birch, M. J. & Miquel, M. E. Speech MRI: Morphology and function. *Physica Medica* **30**(6), 604–618 (2014). doi:10.1016/j.ejmp.2014.05.001.

[8] de Jonge, C. S., Coolen, B. F., Peper, E. S., Motaal, A. G., Nio, C. Y., Somers, I., Strijkers, G. J., Stoker, J. & Nederveen, A. J. Evaluation of compressed sensing MRI for accelerated bowel motility imaging. *Eur. Radiol. Exp.* **3**(1), 7 (2019). doi:10.1186/s41747-018-0079-9.

[9] Lu, K.-H., Liu, Z., Jaffey, D., Wo, J. M., Mosier, K. M., Cao, J., Wang, X. & Powley, T. L. Automatic assessment of human gastric motility and emptying from dynamic 3D magnetic resonance imaging. *Neurogastroenterology & Motility* **34**(1), e14239 (2022). doi:10.1111/nmo.14239.

[10] Pruessmann, K. P., Weiger, M., Scheidegger, M. B. & Boesiger, P. SENSE: Sensitivity encoding for fast MRI. *Magn. Reson. Med.* **42**(5), 952–962 (1999). doi:10.1002/(SICI)1522-2594(199911)42:5<952::AID-MRM16>3.0.CO;2-S.

[11] Griswold, M. A., Jakob, P. M., Heidemann, R. M., Nittka, M., Jellus, V., Wang, J., Kiefer, B. & Haase, A. Generalized autocalibrating partially parallel acquisitions (GRAPPA). *Magn. Reson. Med.* **47**(6), 1202–1210 (2002). doi:10.1002/mrm.10171.

[12] Lustig, M., Donoho, D. & Pauly, J. M. Sparse MRI: The application of compressed sensing for rapid MR imaging. *Magn. Reson. Med.* **58**(6), 1182–1195 (2007). doi:10.1002/mrm.21391.

[13] Feng, L., Grimm, R., Block, K. T., Chandarana, H., Kim, S., Xu, J., Axel, L., Sodickson, D. K. & Otazo, R. Golden-angle radial sparse parallel MRI: Combination of compressed sensing, parallel imaging, and golden-angle radial sampling for fast and flexible dynamic volumetric MRI. *Magn. Reson. Med.* **72**(3), 707–717 (2014). doi:10.1002/mrm.24980.

[14] Otazo, R., Candès, E. & Sodickson, D. K. Low-rank plus sparse matrix decomposition for accelerated dynamic MRI with separation of background and dynamic components. *Magn. Reson. Med.* **73**(3), 1125–1136 (2015). doi:10.1002/mrm.25240.

[15] Tan, F., Zhu, X., Chan, M., Zapala, M. A., Vasanawala, S. S., Ong, F., Lustig, M. & Larson, P. E. Z. Motion-compensated low-rank reconstruction for simultaneous structural and functional UTE lung MRI. *Magn. Reson. Med.* **90**(3), 1101–1113 (2023). doi:10.1002/mrm.29703.

[16] Chen, J., Christodoulou, A. G., Han, P., Xiao, J., Han, F., Hu, Z., Wang, N., Han, H., Ling, D. C., Chang, E. L., Feng, M., Scholey, J. E., Cui, S., Li, D., Yang, W. & Fan, Z. Abdominal MR Multitasking for radiotherapy treatment planning: A motion-resolved and multicontrast 3D imaging approach. *Magn. Reson. Med.* **93**(1), 108–120 (2025). doi:10.1002/mrm.30256.

[17] Yerly, J., Roy, C. W., Milani, B., Eyre, K., Raifee, M. J. & Stuber, M. High on sparsity: Interbin compensation of cardiac motion for improved assessment of left-ventricular function using 5D whole-heart MRI. *Magn. Reson. Med.* **93**(3), 975–992 (2025). doi:10.1002/mrm.30323.

[18] Contijoch, F., Rasche, V., Seiberlich, N. & Peters, D. C. The future of CMR: All-in-one vs. real-time CMR (Part 2). *Journal of Cardiovascular Magnetic Resonance* **26**(1), 100998 (2024). doi:10.1016/j.jocmr.2024.100998.

[19] Ong, F., Zhu, X., Cheng, J. Y., Johnson, K. M., Larson, P. E. Z., Vasanawala, S. S. & Lustig, M. Extreme MRI: Large-scale volumetric dynamic imaging from continuous non-gated acquisitions. *Magn. Reson. Med.* **84**(4), 1763–1780 (2020). doi:10.1002/mrm.28235.

[20] Feng, L. 4D Golden-Angle Radial MRI at Subsecond Temporal Resolution. *NMR in Biomedicine* **36**(2), e4844 (2023). doi:10.1002/nbm.4844.

[21] Olausson, T. E., Terpstra, M. L., Huttinga, N. R. F., Beijst, C., Blanken, N., Suchá, D., Correia, T., Velthuis, B. K., van den Berg, C. A. T. & Sbrizzi, A. Free-running time-resolved first-pass myocardial perfusion using a multi-scale dynamics decomposition: CMR-MOTUS. *Magn. Reson. Mater. Phys.* (2025). doi:10.1007/s10334-025-01291-x.

[22] Chen, C., Liu, Y., Schniter, P., Tong, M., Zareba, K., Simonetti, O., Potter, L. & Ahmad, R. OCMR (v1.0)–Open-Access Multi-Coil k-Space Dataset for Cardiovascular Magnetic Resonance Imaging (2020). doi:10.48550/arXiv.2008.03410.

[23] Wang, C., Lyu, J., Wang, S., Qin, C., Guo, K., Zhang, X., Yu, X., Li, Y., Wang, F., Jin, J., Shi, Z., Xu, Z., Tian, Y., Hua, S., Chen, Z., Liu, M., Sun, M., Kuang, X., Wang, K., Wang, H., Li, H., Chu, Y., Yang, G., Bai, W., Zhuang, X., Wang, H., Qin, J. & Qu, X. CMRxRecon: A publicly available k-space dataset and benchmark to advance deep learning for cardiac MRI. *Sci. Data* **11**(1), 687 (2024). doi:10.1038/s41597-024-03525-4.

[24] van Riel, M. H. C., Heesterbeek, D. G. J., Sheombarsing, R. S. S., Froeling, M., van Leeuwen, T., van den Berg, C. A. T. & Sbrizzi, A. 4D Time-Resolved Strain Tensor Analysis Using Spectro-Dynamic MRI Reveals Muscle Activation Patterns. In *Proc. Intl. Soc. Mag. Reson. Med.*, vol. 33 (2025). doi:10.58530/2025/0982.

[25] Heesterbeek, D. G. J., van Riel, M. H. C., Sheombarsing, R. S. S., van Leeuwen, T., Froeling, M., van den Berg, C. A. T. & Sbrizzi, A. Quantitative in-vivo analysis of biomechanical properties reveals tissue stiffness changes during contraction of the thigh muscles. In *Proc. Intl. Soc. Mag. Reson. Med.*, vol. 33 (2025). doi:10.58530/2025/3203.

[26] Prieto, C., Doneva, M., Usman, M., Henningsson, M., Greil, G., Schaeffter, T. & Botnar, R. M. Highly efficient respiratory motion compensated free-breathing coronary mra using golden-step Cartesian acquisition. *J. Magn. Reson. Imaging* **41**(3), 738–746 (2015). doi:10.1002/jmri.24602.

[27] Li, X., Morgan, P. S., Ashburner, J., Smith, J. & Rorden, C. The first step for neuroimaging data analysis: DICOM to NIfTI conversion. *Journal of Neuroscience Methods* **264**, 47–56 (2016). doi:10.1016/j.jneumeth.2016.03.001.

[28] Rohm, M., Markmann, M., Forsting, J., Rehmann, R., Froeling, M. & Schlaffke, L. 3D Automated Segmentation of Lower Leg Muscles Using Machine Learning on a Heterogeneous Dataset. *Diagnostics* **11**(10), 1747 (2021). doi:10.3390/diagnostics11101747.

[29] Froeling, M. QMRTTools: a Mathematica toolbox for quantitative MRI analysis. *Journal of Open Source Software* **4**(38), 1204 (2019). doi:10.21105/joss.01204.

[30] Inati, S. J., Naegle, J. D., Zwart, N. R., Roopchansingh, V., Lizak, M. J., Hansen, D. C., Liu, C.-Y., Atkinson, D., Kellman, P., Kozerke, S., Xue, H., Campbell-Washburn, A. E., Sørensen, T. S. & Hansen, M. S. ISMRM Raw data format: A proposed standard for MRI raw datasets. *Magn. Reson. Med.* **77**(1), 411–421 (2017). doi:10.1002/mrm.26089.

[31] Blumenthal, M., Heide, M., Holme, C., Juschitz, M., Rapp, B., Schaten, P., Scholand, N., Tamir, J., Tönnes, C. & Uecker, M. mrirecon/bart: version 0.9.00. *Zenodo* (2023). doi:10.5281/zenodo.10277939.